energies

MDPI

Article

SMES-GCSC Coordination for Frequency and Voltage Regulation in a Multi-Area and Multi-Source Power System with Penetration of Electric Vehicles and Renewable Energy Sources

Hiramani Shukla [1], Srete Nikolovski [2,*], More Raju [1,*], Ankur Singh Rana [3] and Pawan Kumar [4]

[1] Electrical Engineering Department, Maulana Azad National Institute of Technology Bhopal, Bhopal 462003, India
[2] Power Engineering Department, Faculty of Electrical Engineering, Computer Science and Information Technology, J. J. Strossmayer University of Osijek, K. Trpimira 2B, HR-31000 Osijek, Croatia
[3] Department of Electrical and Electronics Engineering, National Institute of Technology Tiruchirappalli, Tiruchirappalli 620015, India
[4] Electrical and Instrumentation Engineering Department, Thapar Institute of Engineering and Technology, Patiala 147004, India
* Correspondence: srete.nikolovski@ferit.hr (S.N.); mraju@manit.ac.in (M.R.)

Abstract: Frequency, tie-line power, and the terminal voltages of synchronized generators must all be kept within prescribed limits to ensure the stability of an interconnected power grid through combined automatic generation control (AGC) and automatic voltage regulator (AVR) loops. Thermal power plants, electric vehicles, and renewable energy sources—including solar and wind, geothermal, and solar thermal power plants—form the two-area integrated power system in present research. A new cascade controller named the cascaded proportional integral derivative (PID) and fractional-order PID (CPID-FOPID) controller is proposed for the first time, whose performance is compared with the PID and FOPID controller. The results show that the proposed cascade controller outperforms PID and FOPID in delivering superior dynamic characteristics, including short settling times and low oscillation amplitudes. A new metaheuristic algorithm named the coot algorithm was applied to optimize the parameters of these controllers. The suggested controller outperforms FOPID in the combined AGC and AVR problem under uncertain conditions (random load disturbance, variable input of solar irradiation, and wind power). Robustness of the controller is tested with significant variation in the turbine time constant of the thermal and geothermal power plant. In this study, authors also investigated the best possible coordination between the superconducting magnetic energy storage (SMES) and gate-controlled series capacitor (GCSC) devices to control both voltage and frequency simultaneously. The effect of communication time to the power system is analyzed in this study. Additionally, the obtained results are satisfactorily validated using OPAL-RT real-time digital simulator.

Keywords: automatic generation control (AGC); automatic voltage regulator (AVR); gate-controlled series capacitor (GCSC); superconducting magnetic energy storage (SMES); cascaded controller

Citation: Shukla, H.; Nikolovski, S.; Raju, M.; Rana, A.S.; Kumar, P. SMES-GCSC Coordination for Frequency and Voltage Regulation in a Multi-Area and Multi-Source Power System with Penetration of Electric Vehicles and Renewable Energy Sources. *Energies* **2023**, *16*, 251. https://doi.org/10.3390/en16010251

Academic Editor: Jurgita Raudeliuniene

Received: 20 November 2022
Revised: 21 December 2022
Accepted: 22 December 2022
Published: 26 December 2022

1. Introduction

In an integrated power system having several control zones, power system engineers are primarily concerned with maintaining frequency and voltage levels close to optimal operating conditions. By balancing load demand with generation and related losses, a well-maintained power system is supposed to provide uninterrupted, high-quality power to its customers. In a real-time situation, the load changes continuously, so there exist fluctuations in frequency and voltage. To keep these variations within acceptable limits, each generator needs two control loops: an automatic generation control (AGC) and an automatic voltage regulator (AVR) [1,2].

Frequency and voltage oscillations may become more pronounced and even cause system instability due to the lack of inertia in photovoltaic (PV) systems. Due to the depletion of traditional energy sources, rising fuel costs, and environmental warming conditions, incorporating renewable energy sources (RES) is increasing in the current fossil fuel-based power system. As a substitute to traditional fossil fuels, RES, such as wind power generation (WPG) and solar photovoltaic (SPV) generation, have captured the interest of researchers [1,3–5].

The controlling of the renewable energy sources is challenging since they strongly depend on climate factors. To overcome this issue, storage devices, such as SMES, flywheels, and batteries, can be used in combination with RES to improve grid stability and frequency fluctuations [2,5]. At times of high demand from the grid, these devices release their stored energy. At the same time, non-petroleum-dependent alternatives such as electric vehicles (EVs) are growing in favor as eco-friendly alternatives to traditional gasoline automobiles that can contribute to a greener future.

These EVs have the potential to serve as energy storage devices that aid in frequency regulation as a source during the times of high demand [1]. To address the AGC issue, a few research studies have been conducted on EV penetration [6–10]. Authors in [6,7] analyzed the effect of EV and communication delay on isolated power systems. Utilizing EV for AGC accentuates the reorganized power market [8]. However, research on EV integration for combined AGC and AVR is in its infancy and requires attention [11].

The superconducting magnetic energy storage (SMES) technology can manage both real and reactive power requirements. The SMES system functions as energy-compensating equipment for larger loads and therefore controls frequency oscillations [2,12]. The SMES action is faster than the primary control mechanism of the governor [12]. Frequently charging and discharging of a battery system to handle power system fluctuations reduces its lifespan and performance. The SMES technology is preferable over battery systems [12–14]. However, the superiority of the SMES system in managing the active and reactive powers together having solar PV, wind, geothermal, and thermal power plants is yet to be determined in the presence of a cascaded controller.

Flexible AC transmission system (FACTS) devices enhance the power system's transfer capacity and stability. Series FACTS devices, such as the thyristor-controlled series capacitor (TCSC), the static synchronous series compensator (SSSC), the thyristor-controlled phase shifter (TCPS), the interline power flow controller (IPFC), and the gate-controlled series capacitor (GCSC), demonstrate their efficacy in managing the tie-line powers in AGC [15,16]. Among all FACTS devices, the GCSC has recently captured the attention researchers in AGC studies due to its numerous benefits [16]. The GCSC has a smaller capacitor size, lower cost, and stronger compensating capabilities than the TCSC. The GCSC is simpler and more cost-effective than the TCPS and SSSC [17,18]. References [13,14] have studied the coordination of SMES-TCSC and SMES-SSSC; however, the coordination of SMES with GCSC is not found in the literature addressing combined AGC and AVR loop problems.

In order to regulate the frequency and voltage fluctuations in AGC and AVR loops, suitable controllers are required. Various integer order controllers [2,3,19] and proportional integral derivative (PID) controllers [1,2,11,20–22] have been used in the past to solve AGC and AVR difficulties in literature. Because of its low price, ease of use, and reliability in practice, the PID controller is mostly used in the literature. However, it fails when applied to systems with non-minimum phase [1,11,23,24]. Later, the fractional order PID (FOPID) controllers were successfully implemented to address the AGC and/or AVR [25,26] and demonstrated their superiority over integer order controllers because of their extra knobs for flexible control action. Recently, studies have focused on the cascade control arrangement (CCA) in relation to AGC and/or AVR difficulties [19]. The CCA adds a sensor that helps in reducing the disturbance before it affects the output of the plant.

To improve the performance of a controller, its parameters must be optimally optimized using appropriate metaheuristic algorithms. Shukla et al. [1] used the particle swarm optimization (PSO) algorithm to obtain gains of PID and TID controllers. The authors

of [2,20] used a hybrid algorithm of artificial electric field to get the variables of PID controller. The authors of [3] applied gradient-based optimization (GBO) to optimized integral order controllers. Ramoji and Saikia in [11,23,24] utilized Harris hawks optimization (HHO) in their work. The PSO technique has a tendency to fall into a local optimum in a larger dimensional search space with slow convergence nature [27]. The HHO suffers from the drawbacks such as population diversity and local optima [28].

Inspired by the actions of birds with the same name, a new metaheuristic algorithm called the coot algorithm (CA) was presented recently by Naruei and Keynia [29]. In addition to tackling real-world optimization issues like the design of a pressure spring tension, their analysis demonstrates that the CA outperforms most other optimization methods, suggesting that it be investigated further when creating a controller for the combined AGC and AVR issue. The CA successfully applied to address the unimodal and multimodal test functions. The CA proved its efficiency in solving the problems that have unknown search spaces.

The field of AGC and AVR investigations has the following limitations, according to a careful examination of the literature.

- The AGC and AVR loops control with the utilization of cascaded PID-FOPID controllers tuned by coot technique has not yet been observed.
- The investigations showing the comparative behaviors of cascaded PID-FOPID, FOPID, and PID controllers is not found for the system comprising renewable energy sources and electric vehicles.
- The coordinated performance of GCSC and SMES in regulating frequency and voltage with the cascade PID-FOPID controller is not known.
- Further research is needed on the time-delay effect on the combined AGC and AVR system performance in the presence of a coot-based cascaded PID-FOPID.

The above limitations encourage the authors to investigate them in the present research for combined AGC and AVR issue. Based on the limitations found in the literature review, the following are the novel contributions of this research:

- To examine the comparative performance of cascaded PID-FOPID controllers with PID and FOPID controllers to evaluate the superiority of the proposed controller when optimized with the coot technique.
- To demonstrate the efficiency of a cascaded PID-FOPID controller over FOPID random disturbances and variable solar and wind input.
- To examine the optimal configuration for the application of GCSC and SMES coordination to the combined AGC and AVR problem by comparing SMES-SMES, GCSC, and SMES-GCSC-SMES coordination strategies.
- To investigate the impact of communication delay on frequency and voltage profile in the presence of a cascaded PID-FOPID controller and to suggest a suitable delay margin for the considered interconnected system.
- To validate the stability of CA-based cascaded PID-FOPID controllers against fluctuations in turbine time constants of thermal and geothermal power plants.
- To validate simulation findings using an OPAL-RT 4510 real-time digital simulator.

For the benefit of the reader, a schematic overview of different sources utilized is presented in Figure 1, namely, the reheat thermal power plant (RTPP), geothermal power plant (GTPP), solar thermal power plant (STPP), solar photovoltaic (SPV), and wind turbine generation (WTG) along with electric vehicles. The control system represented in the figure acts as control center. The power and communication networks are also highlighted. Various kinds of power system elements, such as loads and SMES, are also depicted. Table 1 highlights the comparative analysis of previously published articles, including the current manuscript.

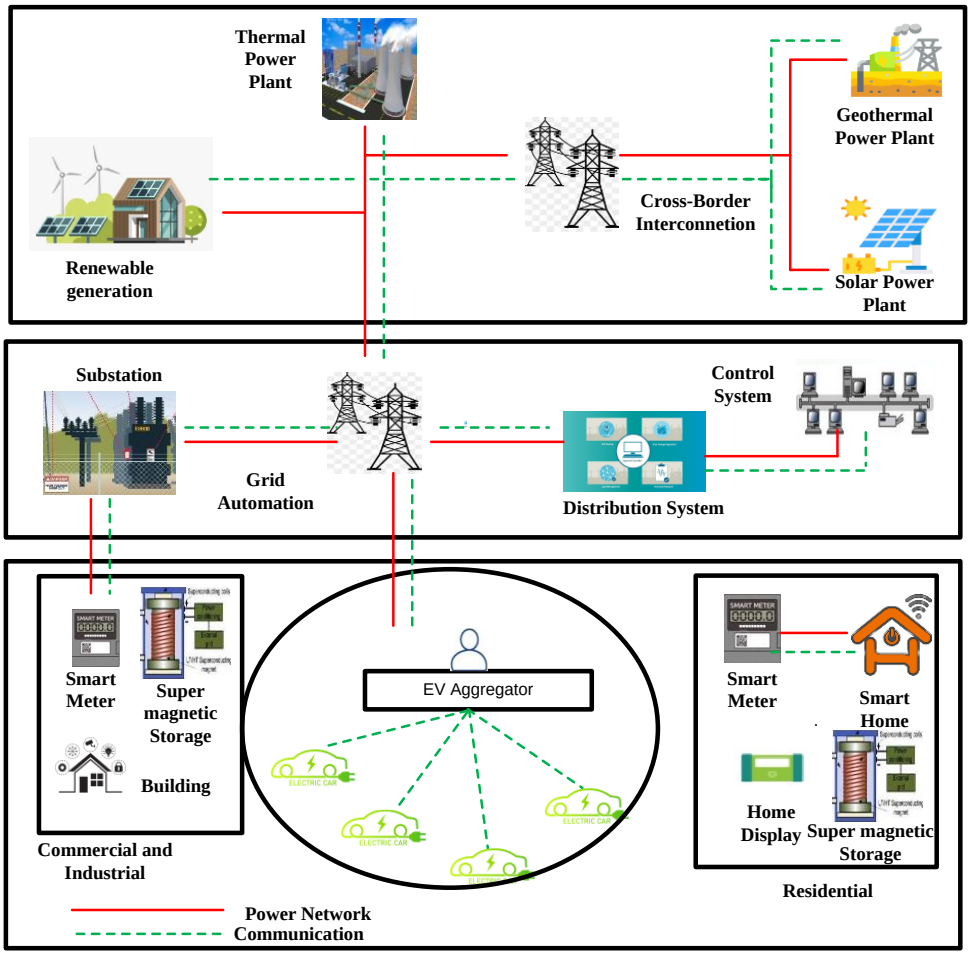

Figure 1. Schematic diagram of sources utilized in the present work.

Table 1. Comparative survey of combined AGC and AVR articles with storage, FACTS, RES and EV integration, and nonlinearities.

Ref.	RES	Energy Storage	EV	FACTS	Nonlinearities
[1]	✔	✖	✖	✖	✔
[2]	✖	✔	✖	✖	✔
[3]	✔	✖	✖	✖	✔
[11]	✖	✖	✔	✖	✔
[19]	✔	✔	✖	✖	✔
[20]	✔	✔	✖	✔	✔
[21]	✔	✔	✖	✖	✖
[22]	✔	✔	✖	✖	✔
[23]	✔	✔	✖	✖	✔
[24]	✖	✖	✖	✖	✔
This Article	✔	✔	✔	✔	✔

The individual segments of this work are structured as follows. Section 2 describes the power systems under investigation. Section 3 discusses the proposed CPID-FOPID controller structure used for frequency and voltage regulation. The coot technique is explained in Section 4. Section 5 discusses the findings for all test systems, along with OPAL-RT validation of the collected results. Finally, the conclusions and recommendations for further study are offered in Section 6.

2. System Investigated

An interconnected two-area power system is taken for investigation having equal sources in both the areas. Small signal analysis is done in this study; thus, the power system's transfer function-based model is represented in Figure 2a,b. The considered system has the following sources in each area: a reheat thermal power plant (RTPP) [1,2], a geothermal power plant (GTPP) [19], and a solar thermal power plant (STPP) [24]. From the renewable energy source (RES), solar photovoltaic (SPV) [1] and wind turbine generation (WTG) [1] are connected in both the areas along with electric vehicles (EVs) [8,9]. All the gain and time constants of the above discussed sources are mentioned in the Appendix A. The system under study is considered an equal area capacity ratio, i.e., 10,000 MW in each area. To make the realistic approach, the system is also incorporated with non-linearities of the reheat turbine, GRC (Figure 2c), and communication time delay. The authors also study the combined coordination effect of FACTS (GCSC) and storage devices (SMES).

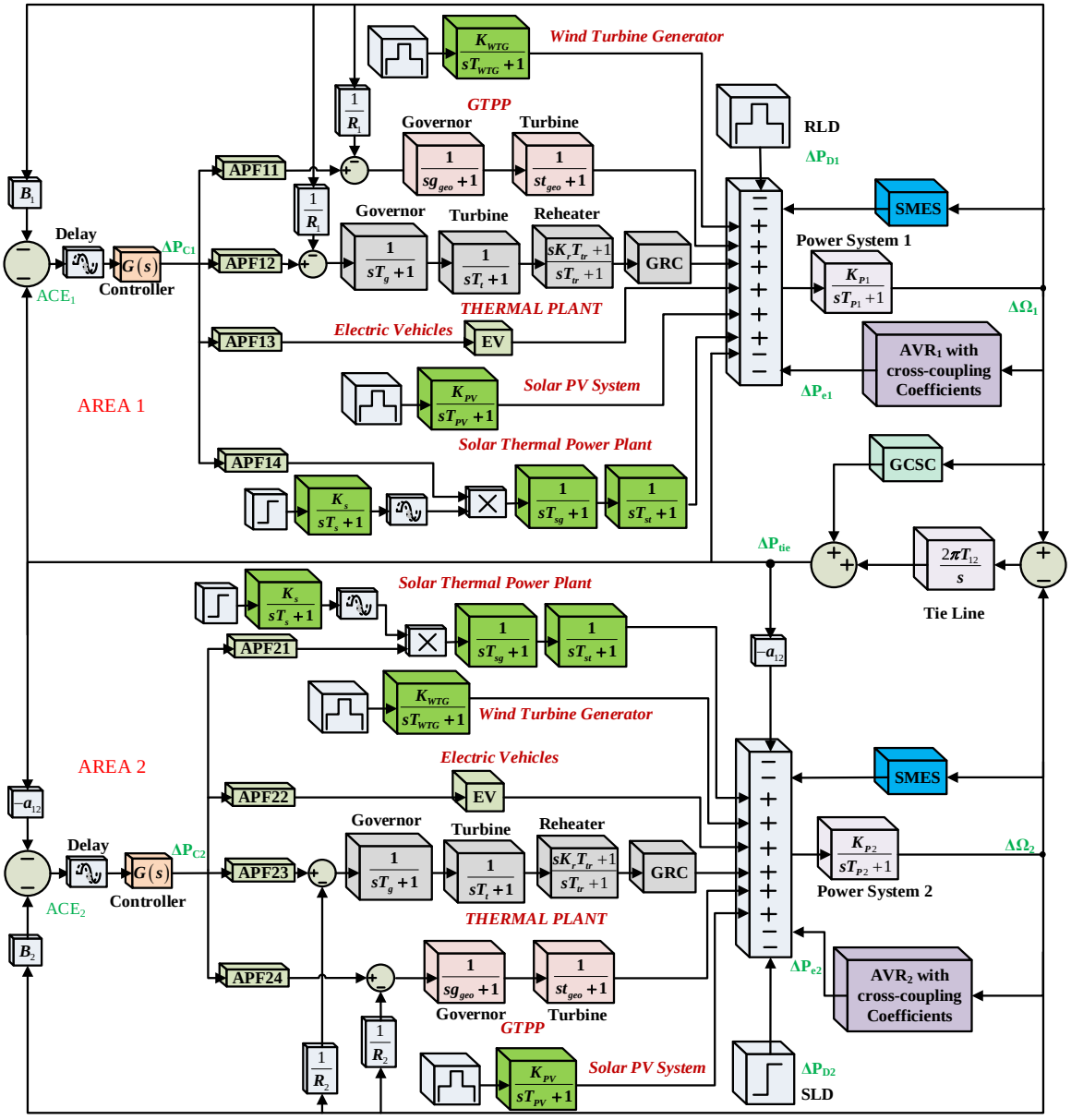

(**a**)

Figure 2. *Cont.*

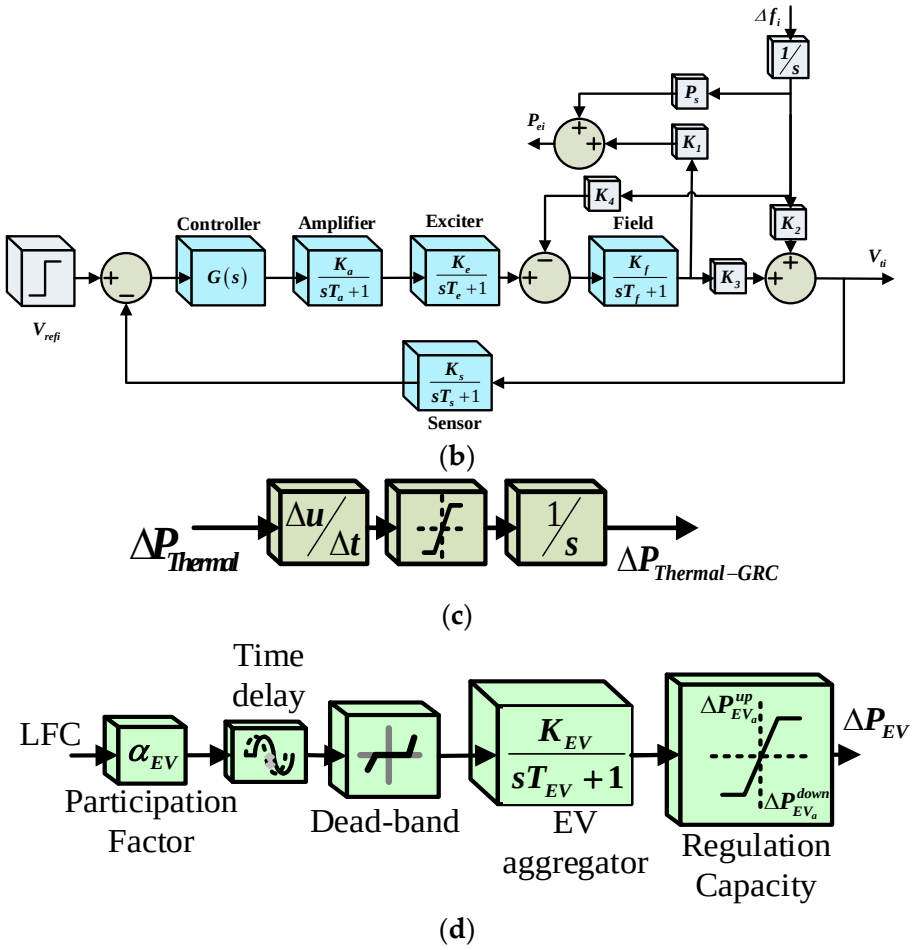

Figure 2. Systems under study: (**a**) interconnected multi-source multi-unit system; (**b**) automatic voltage regulator (AVR) with cross-coupling coefficients; (**c**) GRC nonlinearity; (**d**) electric vehicle (EV) aggregator.

The application of electric vehicles (EVs) is considered in vehicle to gride (V2G) mode. The EVs are comparable to energy storage devices, such as batteries, that may contribute to frequency control [8–10]. A single electric vehicle can produce up to 20 kW [8,9]. Therefore, an EV aggregator is required for AGC and AVR problems that typically include MW-range capacities. EVs often include a dynamic model of an EV aggregator, a time delay, a dead band, and regulating capacity [8,9] (Figure 2d). The maximum and minimum output powers of the EV aggregator are denoted as $\Delta P_{EV_a}^{U}$ and $\Delta P_{EV_a}^{U}$, which are related to incremental generation change (ΔP_{EV}) in any area, as shown in Equation (1).

$$\begin{aligned} \Delta P_{EV_a}^{U} &= {}^{\Delta P_{EV}}/_{N_{EV}} \\ \Delta P_{EV_a}^{D} &= -{}^{\Delta P_{EV}}/_{N_{EV}} \end{aligned} \tag{1}$$

where N_{EV} is the total number of electric vehicles connected to the grid. This study assumed that each EV has the ΔP_{EV} of 5 kW, and there are 8000 numbers of such EVs connected in each area.

3. Controller Structure

To find out the solution of the two-area combined AGC and AVR issue, a cascaded controller is utilized. The primary purpose of the cascaded controller is to improve the disturbance rejection for multi-loop issues like frequency regulation [19]. The two controllers in this setup, designated as $C_1(s)$ and $C_2(s)$, are referred to as the master (M) and slave (S)

controllers, respectively. The control mechanism for the cascade is depicted in Figure 3a, along with $C_1(s)$ and $C_2(s)$.

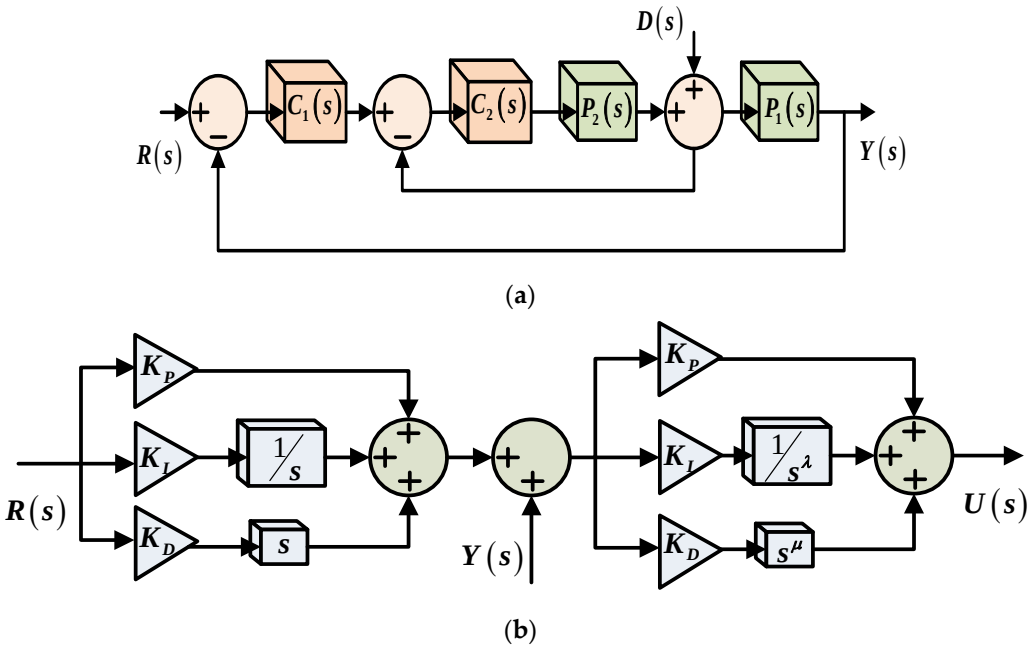

Figure 3. The cascade controller: (**a**) cascade controller mechanism; (**b**) cascade PID-FOPID controller.

Area control error (*ACE*) refers to the error reported to the controller. When system loading changes, frequency, and tie-line powers diverge from their nominal or scheduled values, it is undesirable and can lead to power system failure. Continuous monitoring between load demand and generation in AGC reduces *ACE*. The *ACE* is a linear combination of frequency and tie-line power variations (Equations (2) and (3)).

$$ACE_{\mathbf{1}} = \boldsymbol{\beta_1}\Delta f_{\mathbf{1}} + \Delta P_{tie} \tag{2}$$

$$ACE_{\mathbf{2}} = \boldsymbol{\beta_2}\Delta f_{\mathbf{2}} + a_{\mathbf{12}}\Delta P_{tie} \tag{3}$$

The $\boldsymbol{\beta_1}$ and $\boldsymbol{\beta_2}$ are frequency response characteristics, which are the same as the frequency bias constant (B_i); Δf_1 and Δf_2 are the deviation in area frequency; ΔP_{tie} and $a_{\mathbf{12}}$ are deviation in tie-line power flow and area rating ratio, respectively.

The fractional order is governed by the generalized integer order calculus. This presents the most frequently used integrators and Reimann–Liouville (RL) fractional derivatives in Equations (4) and (5).

$${}_aD_t^{\alpha} f(t) = \frac{1}{\Gamma(q-\alpha)}\frac{d^q}{dt^q}\int_a^t (t-\tau)^{-\alpha-1+q} f(\tau)d\tau,\ \mathrm{q}-1 \le \alpha \le q \tag{4}$$

$${}_aD_t^{-\alpha} f(t) = \frac{1}{\Gamma(\alpha)}\int_a^t (t-\tau)^{\alpha-1} f(\tau)d\tau \tag{5}$$

The terms a, t, D_t^{α}, and $\Gamma(q-\alpha)$ denote initial time instance, final time instance, differential fractional operator, and Euler's gamma function, respectively. The "q" takes the integer values whose rage is $q-1 \le \alpha \le q$.

Specifically, the transfer functions of a cascade combination of PID-FOPID controller is shown in Figure 3b.

$$C_1(s) = G(s)_{PID}^{w} = K_P^w + \frac{K_I^w}{s} + K_D^w s \tag{6}$$

$$C_2(s) = G(s)_{FOPID}^{w} = K_P^w + \frac{K_I^w}{s^{\lambda}} + K_D^w s^{\mu} \tag{7}$$

The terms $G(s)^{w}_{PID}$ and $G(s)^{w}_{FOPID}$ are the master and slave controllers, respectively, with their derivative, integral, and proportional gains representing K^{w}_{D}, K^{w}_{I}, and K^{w}_{P} in area w and corresponding integral and derivative powers of λ and μ, respectively.

Finding a solution within the feasible zone is the goal of optimization problems, which are solved by limiting some objective function chosen for the system. The integral time absolute error (*ITAE*) criterion, as shown in Equation (8), is used as the objective function for the combined AGC and AVR problem under investigation.

$$J_{ITAE-MIN} = \int_{0}^{T} |\Delta f_1 + \Delta f_2 + \Delta P_{tie} + \Delta V_1 + \Delta V_2| t.dt \tag{8}$$

where Δf_w, ΔV_w, and ΔP_{tie} are the fluctuations in frequency, voltage, and transmission lines, respectively. The terms t and T denote time instance and simulation durations, respectively.

4. Coot Algorithm

The coot algorithm (CA) was recently proposed by Nauei and Keynia [29]. It is inspired by the behavior of coots as they seek food on the water's surface. This technique is modelled after the two phases of motion done by coot birds to guide their swarm towards a predetermined destination. In CA, the random population $X_i = x_1, x_2, x_3 \ldots\ldots\ldots, x_n$ serves as the baseline for continuous evaluation against the objective function. Based on four types of motion, the algorithm is formulated below.

4.1. Random Motion

The random motion of the coot at different position $CP(i)$ is given by Equation (9)

$$CP(i) = CP(i) + A \bullet R_2 \bullet (Q - CP(i)) \tag{9}$$

where R_2 is random number $\in$ [0, 1], and A is described by Equation (10) in terms of maximum iterations (*maxitr*).

$$A = 1 - \frac{itr}{max\ itr} \tag{10}$$

4.2. Chain Movement

This movement is implemented by Equation (11) by taking the average position of the two coots $CP(i)$ and $CP(i-1)$.

$$CP(i) = 0.5(CP(i-1) + CP(i)) \tag{11}$$

4.3. Position Adjustment as Per Group Leader

The selection of leader for execution of this position is calculated by Equation (12).

$$K = 1 + (iMOD\ NL) \tag{12}$$

where NL is the total number of leaders and K is the leader index. The next updated position of the coot based on the leader is represented as Equation (13)

$$CP(i) = LP(k) + 2R_1 \cos(2\pi R) \bullet LP(k) - CP(i) \tag{13}$$

where LP is the position of the leader, and R_1 and R are the random numbers between the range of [0, 1] and [−1, 1], respectively.

4.4. Leader Movement

To get the optimal place, the group leader must keep its position update as per Equation (14).

$$\left.\begin{array}{ll} LP(i) = BR_3\cos(2\pi R)\bullet(gBest - LP(i) + gBest) + gBest & R_4 < 0.5 \\ LP(i) = BR_3\cos(2\pi R)\bullet(gBest - LP(i) + gBest) - gBest & R_4 \geq 0.5 \end{array}\right\} \quad (14)$$

where $gBest$ is the overall best solution, and R_3 and R_4 are random numbers in the range [0, 1]. The B is found using Equation (15).

$$B = 2 - \frac{itr}{max\ itr} \quad (15)$$

For this study, the number of search agents (n) is set to 10, and the number of iterations ($max\ itr$) is taken to 100 to optimize all the controller parameter subjected to Equation (8).

5. Results Analysis

This research work is conducted on a Windows 10Pro PC running with MATLAB/SIMULINK 2016a, with an Intel core i7-8700 CPU, 3.2 GHz clock speed, and 8 GB RAM. Improved results for the cascade controller are emphasized in bold.

5.1. At Nominal Conditions

This study evaluates the combined AGC and AVR for two equal 1000 MW power systems, as depicted in Figure 1a. In this case, 2% step load perturbated (SLP) disturbance is used in both areas (i.e., ΔPD_1 = ΔPD_2 = 1000 MW 0.02 = 20 MW at t = 0 s). In both areas, the geothermal power plant (GTPP), reheat thermal power plant (RTPP) with GRC, wind turbine generator, photovoltaic system, and electric vehicle (EV) are considered for power generation. Different secondary controllers, namely proportional integral derivative (PID), fractional order PID (FOPID), and cascaded PID-FOPID, are utilized to examine the system. To get the parameters of these controllers, the coot algorithm (CA) is used, and the results are subjected to Equation (8).

The J_s ($ITAE$) value for the PID controller is 3.42, while it is 2.155 for the FOPID controller and 1.156 for the cascaded PID-FOPID controller. This shows that the cascaded controller is better than the PID and FOPID controllers in respect to J_s.

The coot algorithm is executed for each controller in order to obtain its parameters. The parameters of the controller (PID, FOPID, and cascaded PID-FOPID) obtained by the CA are shown in Tables 2–4. Figure 4 illustrates the system dynamics for frequency variation in area 1 and 2 (i.e., Δf_1 and Δf_1), change in tie line power (ΔP_{tie}), and pu terminal voltage for AVR 1 and 2 (i.e., V_{t1} and V_{t2}).

Table 2. PID parameters.

Parameters	Area 1	Area 2	AVR 1	AVR 2
K_P	0.9024	0.2601	0.2099	0.3999
K_I	1	0.0999	1	0.9921
K_D	0.9789	0.9101	0.7993	0.1399

Table 3. FOPID parameters.

Parameters	Area 1	Area 2	AVR 1	AVR 2
K_P	0.8515	0.4521	0.1252	0.0743
K_I	0.9064	0.5269	0.674	0.9587
λ	1	0.3402	0.9029	0.9845
K_D	0.8239	0.8501	0.4545	0.6265
μ	0.4423	0.3594	0.9641	0.0196

Table 4. CPID-FOPID parameters.

Parameters	Area 1	Area 2	AVR 1	AVR 2
K_P	0.4243	0.2612	0.8001	0.6867
K_I	0.7488	0.3012	0.9131	0.9786
K_D	1	0.9361	0.0415	0.1074
K_P	0.9808	1	0.332	0.1
K_I	0.1881	0.2004	0.1991	0.5339
λ	0.8667	0.5916	1	0.5001
K_D	0.6615	0.0018	0.801	0.6131
μ	0.6066	0.6502	0.5855	0.001

Evaluation of Figure 4 is shown in Tables 5 and 6, with comparisons made between peak overshoot (M_P), peak undershoot (U_P), and settling time (T_s). The following is a critical analysis of the cascaded controller, based on Table 5: The M_P values for Δf_1, Δf_2, and ΔP_{tie} are 0.00148 Hz, 0.001068 Hz, and 0.00381 puMW, respectively. The U_P values are 0.03485 Hz, 0.0432 Hz, and 0.00177 puMW, and the *Ts* values are 13.55 s, 12.16 s, and 24.11 s, respectively.

The cascaded controller for AVR1 (Table 6) provides an M_P value of **1.02** pu, which is 39.29% better than PID and 14.35% better than FOPID, while the cascaded controller for AVR2 yields an M_P value of **1.063** pu, which is 35.18% better than PID and 32.72% better than FOPID. The settling times (T_s) for the cascaded controller, PID, and FOPID are **14.2 s**, 16.33 s, and 38.98 s for AVR 1, and **11.87 s**, 15.26 s, and 20.98 s for AVR 2, repectively. Therefore, the cascaded PID-FOPID is superior to PID and FOPID in terms of M_P, U_P, and T_s for the combined AGC and AVR problem.

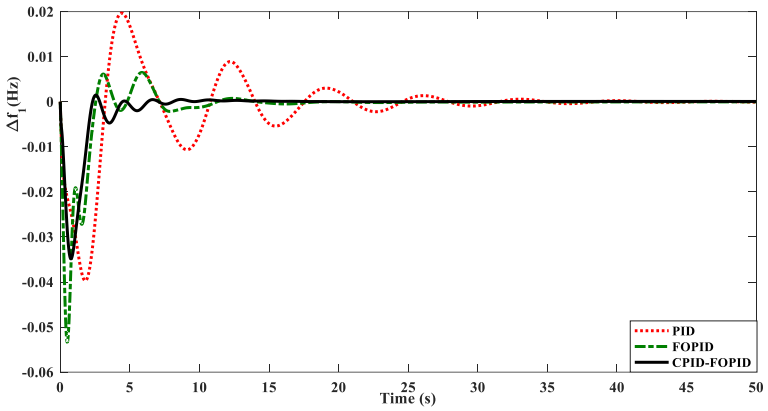

(**a**)

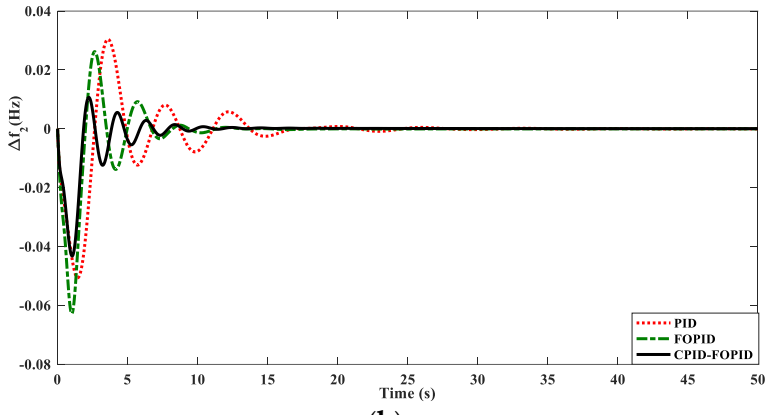

(**b**)

Figure 4. *Cont.*

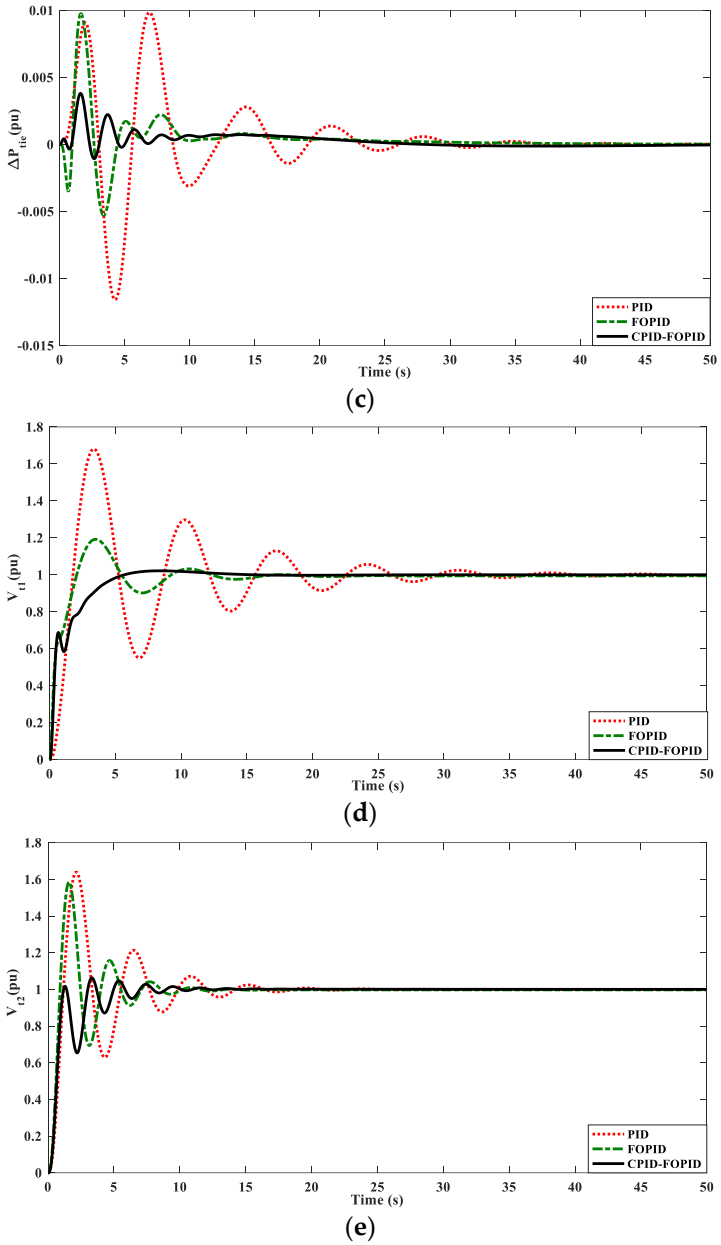

Figure 4. Dynamic responses of different controllers: (**a**) Δf_1; (**b**) Δf_2; (**c**) ΔP_{tie}; (**d**) V_{t1}; (**e**) V_{t2}.

Table 5. Numerical values of $T_s(s)$, M_P, and U_P for AGC.

Controller	Parameters	$\Delta f_1(Hz)$	$\Delta f_2(Hz)$	$\Delta P_{tie}(pu)$
PID	Peak Overshoot (in $10^{\wedge(-3)}$)	19.68	30.4	9.84
	Peak Undershoot (in $10^{\wedge(-3)}$)	39.71	53.13	6.45
	Settling Time(s)	44.33	26.56	42.46
FOPID	Peak Overshoot (in $10^{\wedge(-3)}$)	6.505	26.22	9.75
	Peak Undershoot (in $10^{\wedge(-3)}$)	53.35	62	3.38
	Settling Time(s)	17.2	16.32	35.89
CPID-FOPID	Peak Overshoot (in $10^{\wedge(-3)}$)	**1.48**	**10.68**	**3.81**
	Peak Undershoot (in $10^{\wedge(-3)}$)	**34.85**	**43.2**	**1.77**
	Settling Time(s)	**13.55**	**12.16**	**24.11**

Table 6. Numerical values of $T_s(s)$, M_P, and U_P for AVR.

Controller	Parameters	V_{t1} (*pu*)	V_{t2} (*pu*)
PID	Peak Overshoot	1.68	1.64
	Peak Undershoot	NIL	NIL
	Settling Time(s)	38.98	20.91
FOPID	Peak Overshoot	1.191	1.58
	Peak Undershoot	NIL	NIL
	Settling Time(s)	16.33	15.26
CPID-FOPID	Peak Overshoot	**1.02**	**1.063**
	Peak Undershoot	**NIL**	**NIL**
	Settling Time(s)	**14.2**	**11.87**

5.2. Effect of Random Load Demand (RLD), Variable Solar Irradiations, and Irregular Wind Power

The studies done so far have assumed constant solar irradiances and wind power, as well as a 2% step disturbance. However, under realistic conditions, these vary continuously. To evaluate this circumstance, the random load demand (RLD), variable solar irradiations, and irregular wind power depicted in Figure 5 are considered. The performance of the proposed cascade controller is compared to that of the FOPID controller after parameters are obtained via the coot algorithm (Tables 7 and 8). When using the proposed coot-based cascade controller, the overshoots (M_P) and undershoots (U_S) are reduced to a greater extent than they are with the FOPID controller. This is an indication of the superiority of the cascade controller. The dynamics (i.e., Δf_1, Δf_2, ΔP_{tie}, V_{t1}, and V_{t2}) are depicted in Figure 6.

Table 7. FOPID controller gain for RLD, variable solar irradiations, and irregular wind power.

Parameters	Area 1	Area 2	AVR 1	AVR 2
K_P	0.6646	0.6166	0.7214	0.1512
K_I	0.4053	0.0967	0.9478	0.3430
λ	0.9998	0.1003	0.9711	1.0010
K_D	0.2158	0.6907	0.6773	0.1300
μ	0.6742	0.8491	0.4448	0.8131

Table 8. Cascaded PID-FOPID controller gain for RLD, variable solar irradiations, and irregular wind power.

Parameters	Area 1	Area 2	AVR 1	AVR 2
K_P	0.5630	0.9588	0.2273	0.1958
K_I	0.5406	0.5524	0.5665	0.4288
K_D	0.8272	0.0029	0.3829	0.4171
K_P	0.9879	0.0891	0.8746	0.0695
K_I	0.7491	0.8894	1.0101	0.8285
λ	0.7514	0.4316	0.8012	0.9021
K_D	0.5599	0.5101	0.3457	0.9756
μ	0.1893	0.6518	0.3436	0.6042

5.3. Sensitivity Analysis

It is anticipated that the operating circumstances of the power system will vary continuously, and the controller gains must be capable of adapting the system performance for these fluctuations. The sensitivity analysis is performed to validate the capacity of the controller's nominal parameters to perform their function. In this scenario, the time constants of the turbines of RTPP and GTPP are modified by $\pm 30\%$ of both areas. The system dynamics (i.e., Δf_1, Δf_2, ΔP_{tie}, V_{t1}, and V_{t2}) are compared for with and without varied conditions in Figure 7. It can be observed from this comparison that the responses are nearly same, which demonstrates the robustness of the cascade controller with same parameters obtained at nominal conditions.

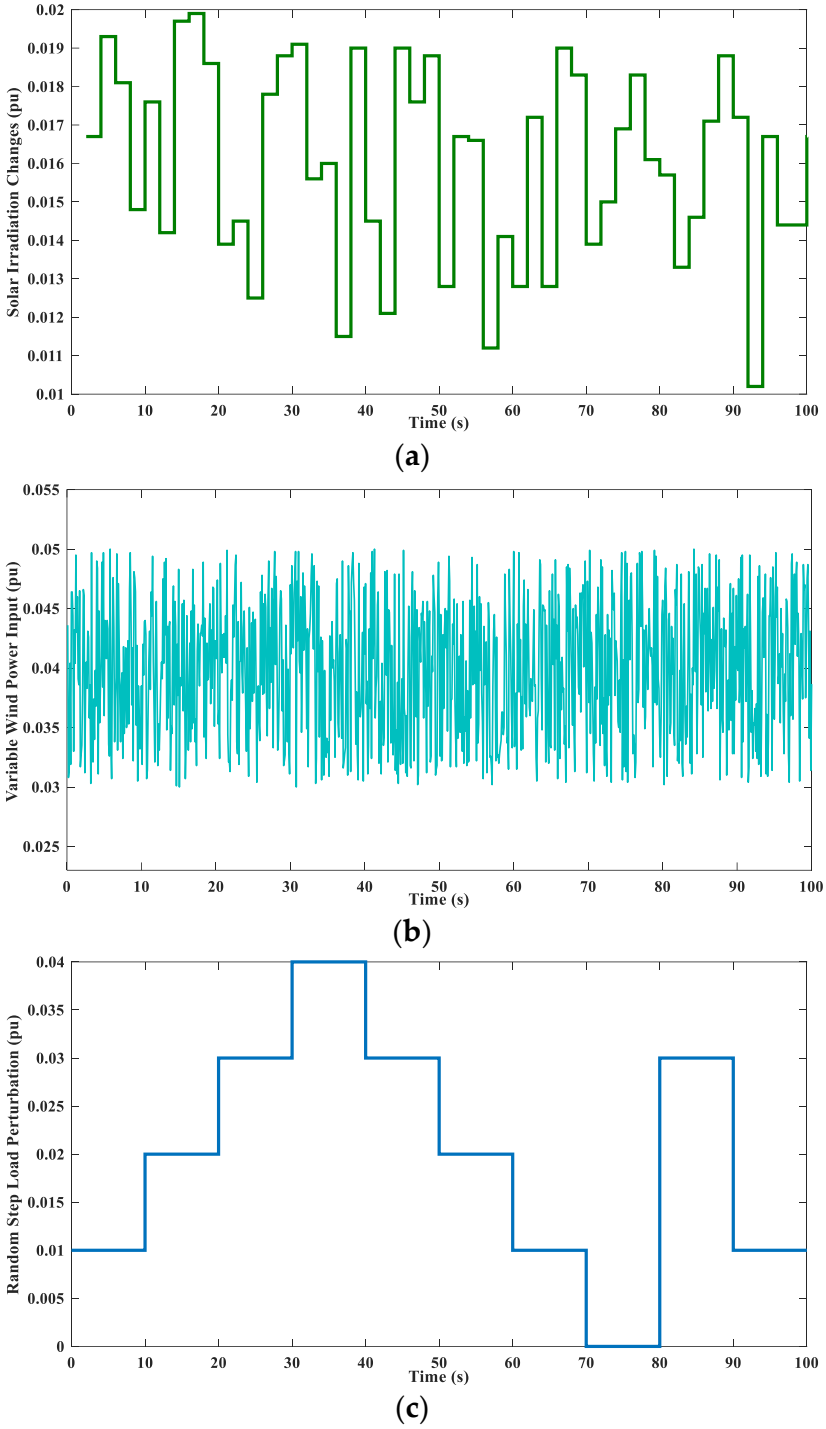

Figure 5. Random patterns of: (**a**) load demand, (**b**) wind power input, and (**c**) solar irradiance.

5.4. SMES-GCSE-SMES Coordination

The superconducting magnetic energy storage (SMES) technology stores electrical power from the grid as the magnetic field of a coil composed of superconducting wire with almost negligible energy loss. Although secondary control actions are slow to respond, the SMES system can improve the system's dynamic behavior and power flow [12–14].

The SMES system incorporates a step-down transformer, as well as an AC/DC converter, a superconducting inductor, and a converter unit. Figure 8 illustrates the schematic diagram of the SMES.

Figure 9 is a representation of its corresponding transfer function model. In this figure, K_{SMES} and T_{SMES} stand for the gains and time constants, respectively. The lead-lag compensation block parameters are expressed by the terms T_1, T_2, T_3, and T_4, respectively. The SMES units are placed at the load points of areas 1 and 2. Notations in the SMES, such as K_{SMES}, T_{SMES}, T_1, T_2, T_3, and T_4, are tuned along with the parameters of the cascaded controller for the purpose of achieving its best possible design. Equation (16) describes the transfer function of the SMES system.

$$TF_{SMES} = \frac{\Delta P_{SMES}}{\Delta f} \frac{(1+sT_1)}{(1+sT_2)} \frac{(1+sT_3)}{(1+sT_4)} \frac{(K_{SMES})}{(1+sT_{SMES})} \tag{16}$$

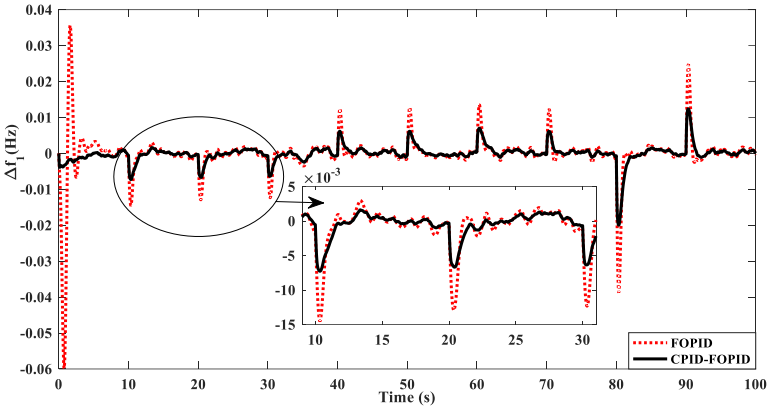

(**a**)

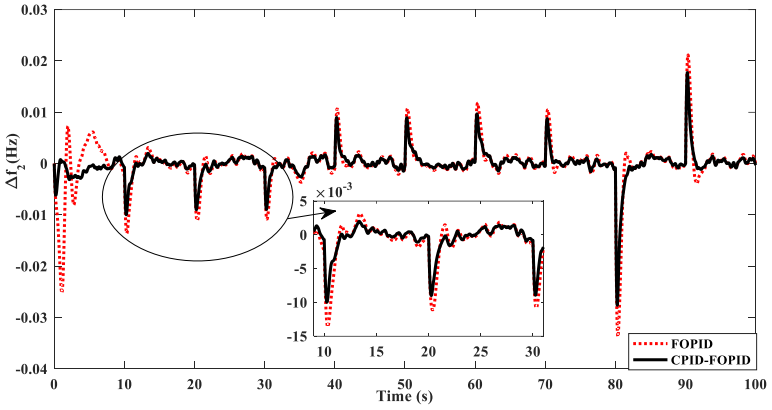

(**b**)

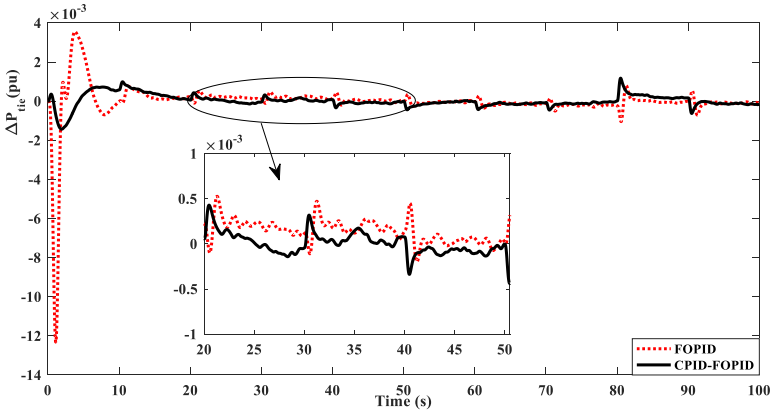

(**c**)

Figure 6. *Cont.*

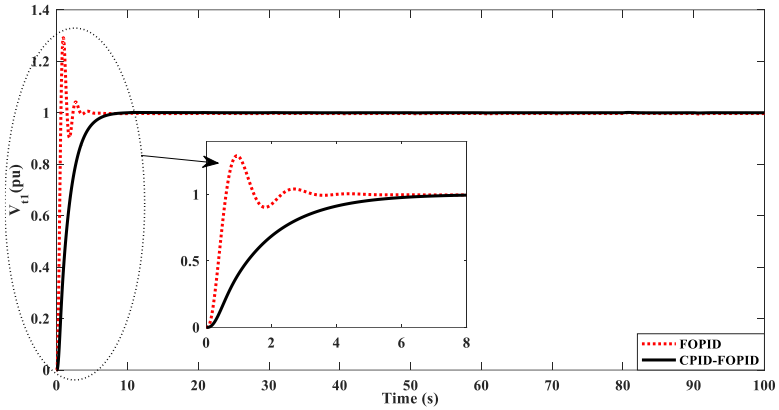

(**d**)

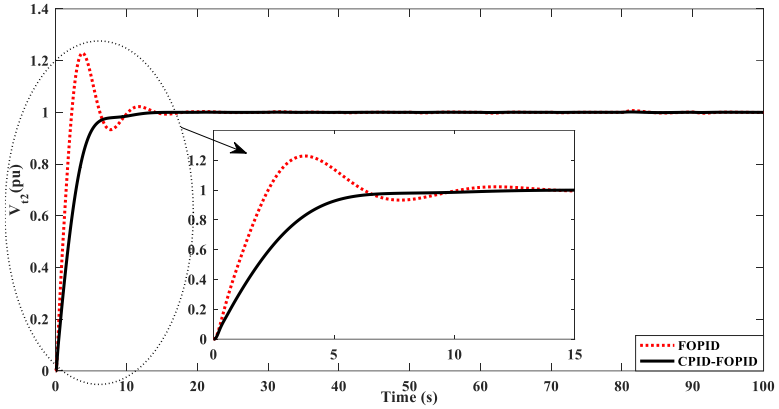

(**e**)

Figure 6. Dynamic responses with random patterns (**a**) Δf_1; (**b**) Δf_2; (**c**) ΔP_{tie}; (**d**) V_{t1}; (**e**) V_{t2}.

The gate-controlled series capacitor (GCSC), which is a series FACTS device based on a pair of gate-commutated switches in parallel with a capacitor, can control the power flow of the transmission lines and its impedance. The schematic diagram is shown in Figure 10.

This article represents different coordination of the above discussed SMES and GCSC. The purpose of this section is to find the best coordination from SMES-SMES, GCSC, and SMES-GCSC-SMES. Table 9 represents gain obtained by the cascaded controller when optimized with CA for SMES-SMES coordination, and Table 10 indicates the optimized values of SMES for this case. Table 11 represents gain obtained by the cascaded controller when optimized with CA for GCSC coordination. Tables 12 and 13 represent gain obtained by the cascaded controller when optimized with CA for SMES-GCSC-SMES coordination and optimized SMES parameters for this case, respectively.

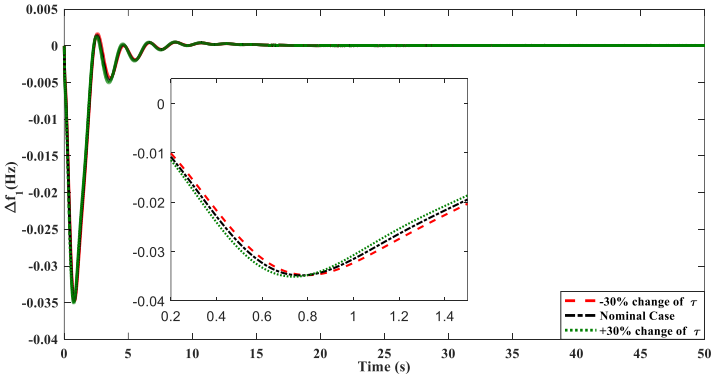

(**a**)

Figure 7. *Cont.*

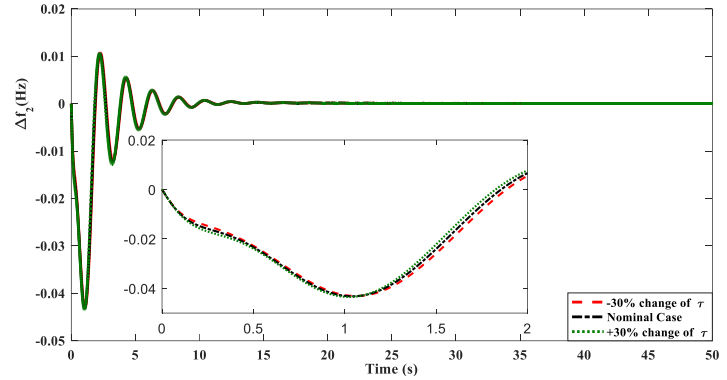

(**b**)

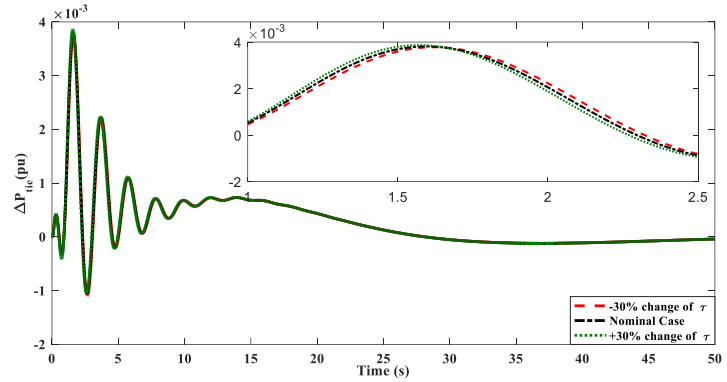

(**c**)

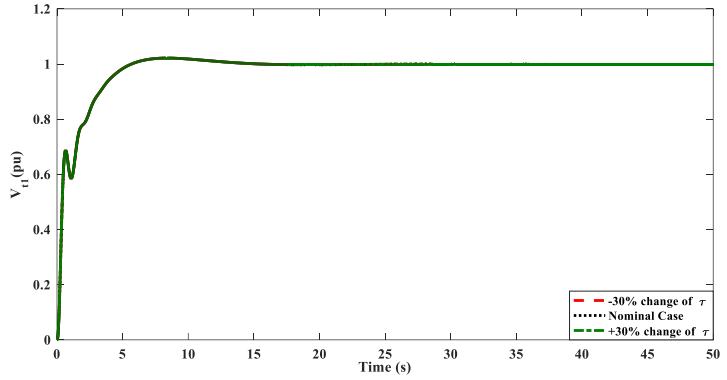

(**d**)

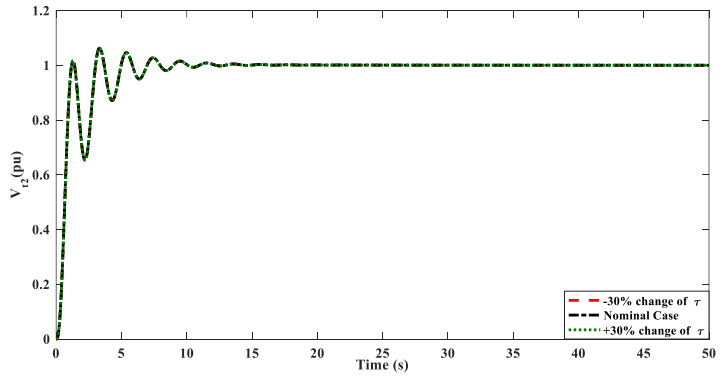

(**e**)

Figure 7. Dynamic responses with insensitive of turbine time constant (τ) of RTPP and GTPP of both the areas: (**a**) Δf_1; (**b**) Δf_2; (**c**) ΔP_{tie}; (**d**) V_{t1}; (**e**) V_{t2}.

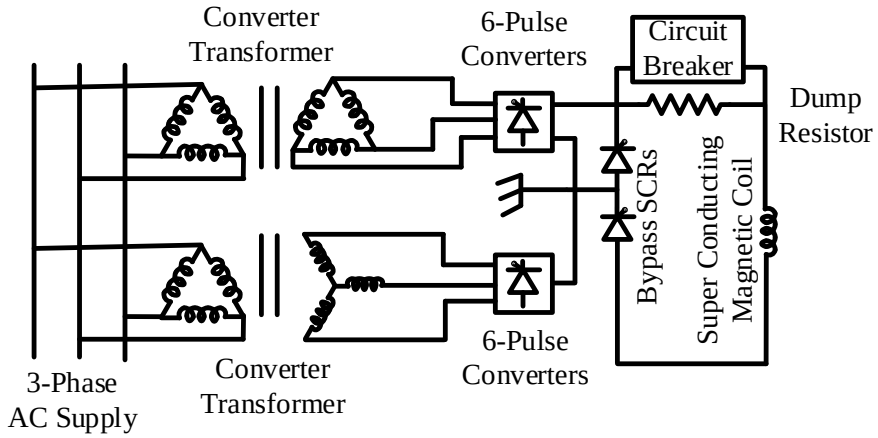

Figure 8. SMES circuit diagram.

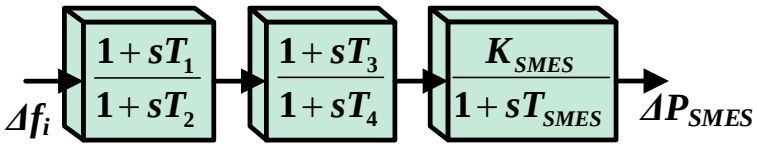

Figure 9. Transfer function-based circuit diagram of SMES.

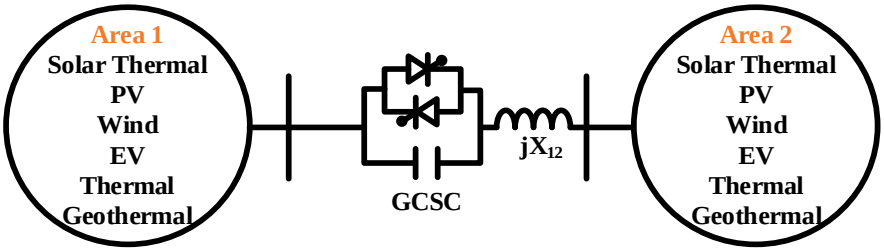

Figure 10. GCSC arrangement in the series of the transmission line.

Table 9. Cascaded PID-FOPID controllers' gain for SMES-SMES coordination.

Parameters	Area 1	Area 2	AVR 1	AVR 2
K_P	0.2258	0.8173	0.3613	0.1791
K_I	0.3065	0.8786	0.9529	0.7979
K_D	0.0856	0.1181	0.4614	0.5346
K_P	0.6511	0.6584	0.8268	0.8311
K_I	0.6122	0.7543	0.6181	1
λ	0.1001	0.1626	0.8967	0.8407
K_D	1	0.4325	0.8971	0.0019
μ	0.0576	0.7115	0.5134	0.1044

Table 10. SMES-optimized parameters for SMES-SMES coordination.

Parameters	SMES 1	SMES 2
T_1	0.0335	0.0501
T_2	0.0932	0.1001
T_3	0.3998	0.5
T_4	0.0173	0.0166
K_{SMES}	0.2986	0.627
T_{SMES}	0.5229	0.01

Figure 11 represents the comparison of system dynamics (i.e., Δf_1, Δf_2, ΔP_{tie}, V_{t1}, and V_{t2}) with the different coordination scheme with nominal case. Among these, coordination SMES-GCSC-SMES found the best results, which is also proven by Tables 14 and 15, with comparisons made between O_P, U_P, and T_s.

Table 11. Cascaded PID-FOPID controllers' gain for GCSC coordination.

Parameters	Area 1	Area 2	AVR 1	AVR 2
K_P	0.6426	0.4157	0.2335	0.2631
K_I	0.9936	0.8508	0.6443	0.8527
K_D	0.8534	0.366	0.9774	0.515
K_P	0.001	0.5467	0.0711	0.7847
K_I	0.2646	0.7844	0.9999	0.8062
λ	0.0943	0.5073	0.8933	0.6129
K_D	0.4109	0.5326	0.1228	0.3681
μ	0.1001	0.6842	0.2966	0.8405

Table 12. Cascaded PID-FOPID controllers' gain for SMES-SMES-GCSC coordination.

Parameters	Area 1	Area 2	AVR 1	AVR 2
K_P	0.9903	0.7472	0.2788	0.5704
K_I	0.2046	0.8415	0.5147	0.6733
K_D	0.9598	0.849	0.8231	0.5776
K_P	0.9048	0.9927	0.1897	0.2183
K_I	0.6968	0.9696	0.6823	0.3916
λ	0.3755	0.0379	1	0.8961
K_D	1	0.9875	0.2716	0.2653
μ	0.2539	0.3412	0.1291	0.0869

Table 13. SMES-optimized parameters for SMES-GCSE-SMES coordination.

Parameters	SMES 1	SMES 2
T_1	0.0396	0.0122
T_2	0.0754	0.0642
T_3	0.4962	0.2332
T_4	0.0298	0.0249
K_{SMES}	0.1278	0.037
T_{SMES}	0.3224	0.1283

Table 14. Numerical values of $T_s(s)$, M_P, and U_P for AGC.

Coordination	Parameters	Δf_1 (*Hz*)	Δf_2 (*Hz*)	ΔP_{tie} (*pu*)
SMES-SMES	Peak Overshoot (in $10^{\wedge(-3)}$)	0.34	NIL	0.31
	Peak Undershoot (in $10^{\wedge(-3)}$)	26.6	18.42	7.966
	Settling Time(s)	12.89	7.12	21.12
GCSC	Peak Overshoot (in $10^{\wedge(-3)}$)	0.66	NIL	1.304
	Peak Undershoot (in $10^{\wedge(-3)}$)	15.72	19.85	12.35
	Settling Time(s)	10.22	6.92	23.93
SMES-GCSC-SMES	Peak Overshoot (in $10^{\wedge(-3)}$)	**NIL**	**NIL**	**NIL**
	Peak Undershoot (in $10^{\wedge(-3)}$)	**12.31**	**16.9**	**7.962**
	Settling Time(s)	**8.91**	**6.78**	**16.87**

Table 15. Numerical values of T_s (*s*), M_P, and U_P for AVR.

Coordination	Parameters	V_{t1} (*pu*)	V_{t2} (*pu*)
SMES-SMES	Peak Overshoot	1.016	1.024
	Peak Undershoot	NIL	NIL
	Settling Time(s)	11.25	8.10
GCSC	Peak Overshoot	1.054	1.018
	Peak Undershoot	NIL	NIL
	Settling Time(s)	9.30	9.26
SMES-GCSC-SMES	Peak Overshoot	**NIL**	**NIL**
	Peak Undershoot	**NIL**	**NIL**
	Settling Time(s)	**7.21**	**7.84**

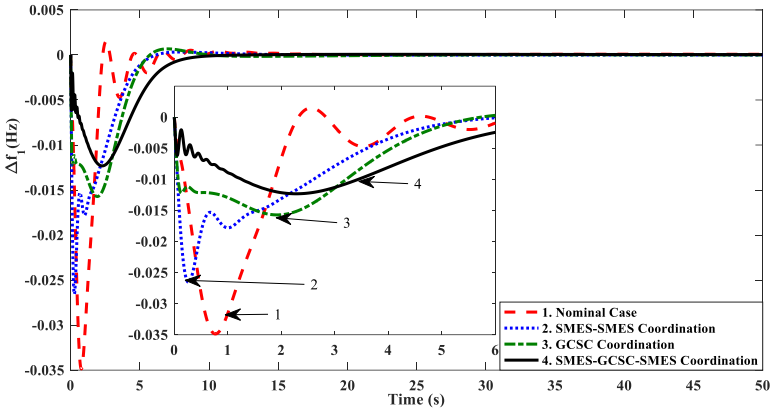

(**a**)

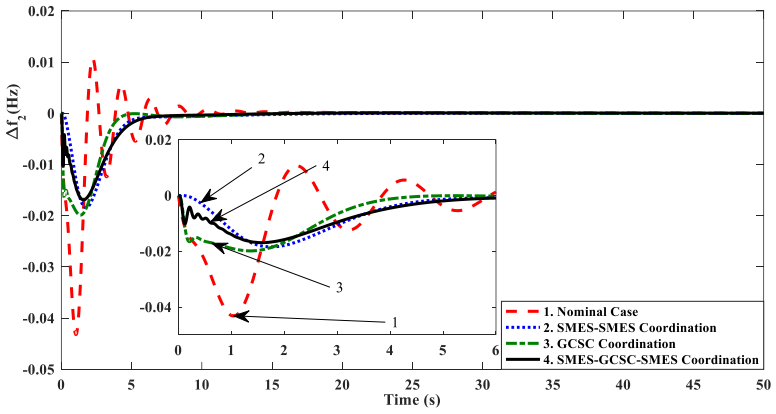

(**b**)

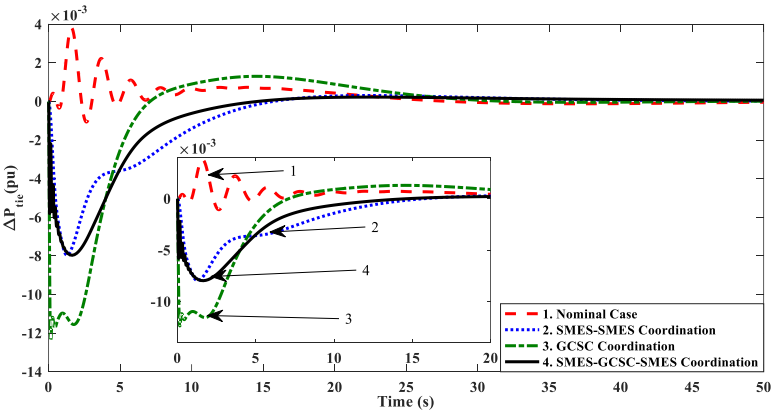

(**c**)

Figure 11. *Cont.*

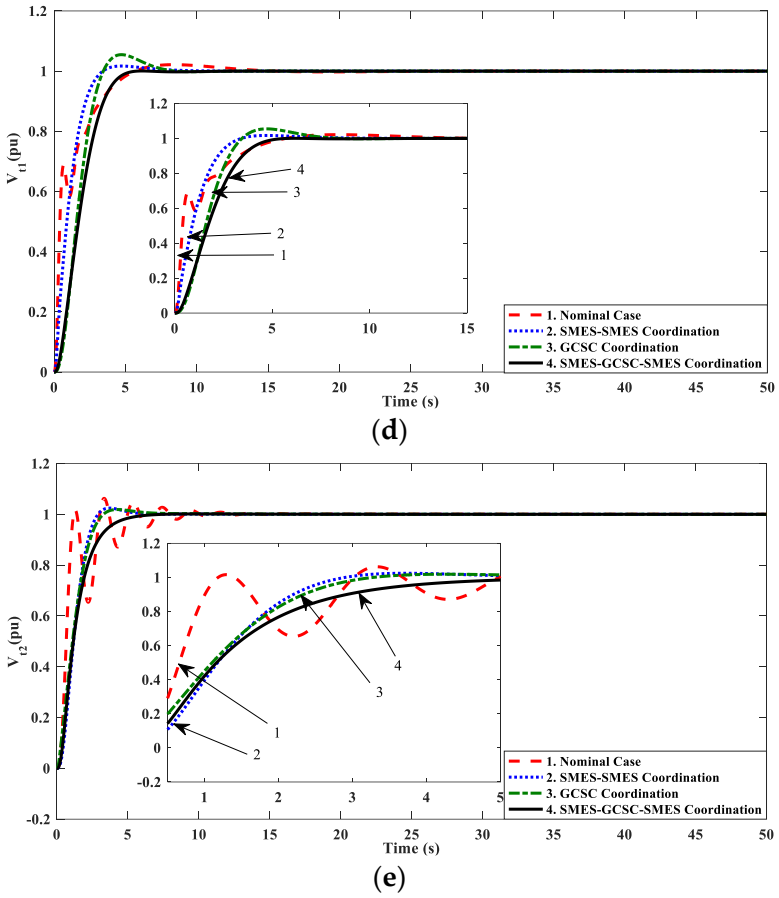

Figure 11. Dynamic responses with different case of GCSC and SMES coordination's: (**a**) Δf_1; (**b**) Δf_2; (**c**) ΔP_{tie}; (**d**) V_{t1}; (**e**) V_{t2}.

5.5. Effect of Communication Time Delay

It is believed that the control signal travels with a certain delay from the distant location to the control center. As a result of these delays, the dynamic behaviors degrade. For this study, the controller receives a single delay signal representing the whole communication delay. Different communication time delays (T_d) are placed on the system, and the dynamics (i.e., Δf_1, Δf_2, ΔP_{tie}, V_{t1}, and V_{t2}) of the system (shown in Figure 12) are studied to see how well the controller works. As shown in Figure 12, as the T_d value rises, the system dynamics are affected by an increase in oscillations.

Up to T_d = 1.6 s, the system dynamics are well-settled, but after applying a delay longer than 1.6 s, the dynamics degrade in nature, and at T_d = 1.85 s, the fluctuations increase and oscillate continuously. The system dynamics become more oscillatory as T_d increases, which is 1.85 s or more. Therefore, for the proposed system to operate reliably, a delay of less than 1.85 s is recommended. The optimized gain of the cascaded controllers obtained at delay of 1.6 s and 1.85 s are mentioned in Tables 16 and 17, respectively.

Table 16. Cascaded PID-FOPID controllers' gain for delay at T_d = 1.6 s.

Parameters	Area 1	Area 2	AVR 1	AVR 2
K_P	0.1045	0.0641	0.5801	0.3867
K_I	0.1597	0.1003	0.9131	0.9786
K_D	0.0415	0.0283	0.0415	0.1074
K_P	0.2661	0.5048	0.0332	0.0911
K_I	0.0238	0.1047	0.7199	0.9533
λ	0.4321	0.5022	0.9754	0.4998
K_D	0.1049	0.0377	0.8991	0.9613
μ	0.4896	0.1501	0.0885	0.1001

5.6. Validaton of the Dynamics through OPAL-RT

The proposed automatic voltage regulator (AVR) and automatic generator controller (AGC) system for two-area power plants is verified on the OPAL-RT OP4510 real-time digital simulator, which makes use of the most up-to-date Intel generation Xeon 4-core processors and a robust Xilinx Kintex-7 FPGA platform. It is capable of real-time parallel processing, producing results that are matched with those obtained on hardware [23,24]. Figure 13 depicts the OPAL-RT OP4510 system in its laboratory configuration, which includes a host PC running RT-Lab software, I/O ports, TCP/IP connection, and the real-time digital simulator itself. In order to validate the proposed unified ALFC and AVR control pattern, it is first constructed in the MATLAB/Simulink R2018 platform. The technique combines the parallel processing power of the real-time simulator. The results from the system are compared to the results from using MATLAB. In-depth analysis of the results (Figure 14) shows that the system outputs (i.e., Δf_1, Δf_2, ΔP_{tie}, V_{t1}, and V_{t2}) on both platforms are quite equivalent, lending support to the validity of the suggested method.

Table 17. Cascaded PID-FOPID controllers' gain for delay at T_d = 1.85 s.

Parameters	Area 1	Area 2	AVR 1	AVR 2
K_P	0.8095	0.5084	0.7536	0.7011
K_I	0.4037	0.3062	0.8041	0.6089
K_D	0.1006	0.0354	0.1158	0.0668
K_P	0.0805	0.2055	0.7066	0.1218
K_I	0.5701	0.0172	0.8181	0.9835
λ	0.7671	0.1221	0.3099	0.4013
K_D	0.0652	0.0281	0.9501	0.2071
μ	0.0367	0.1339	0.0266	0.0575

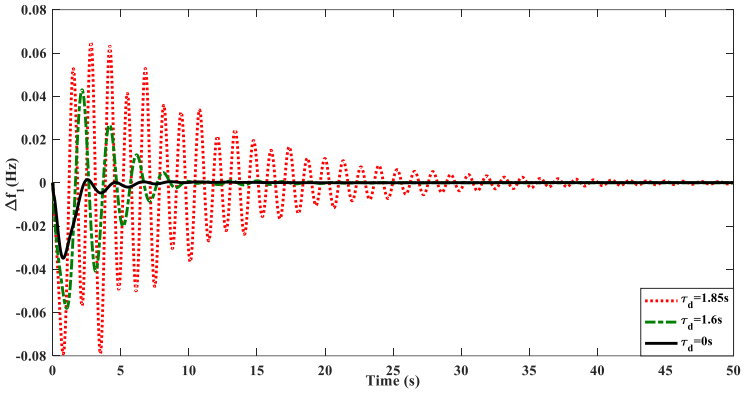

(**a**)

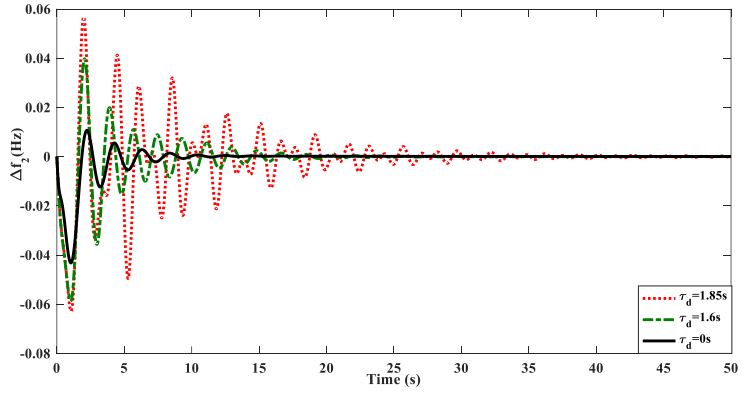

(**b**)

Figure 12. *Cont.*

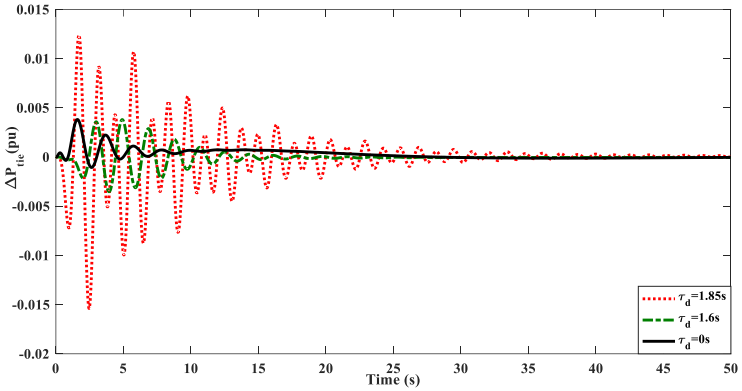

(**c**)

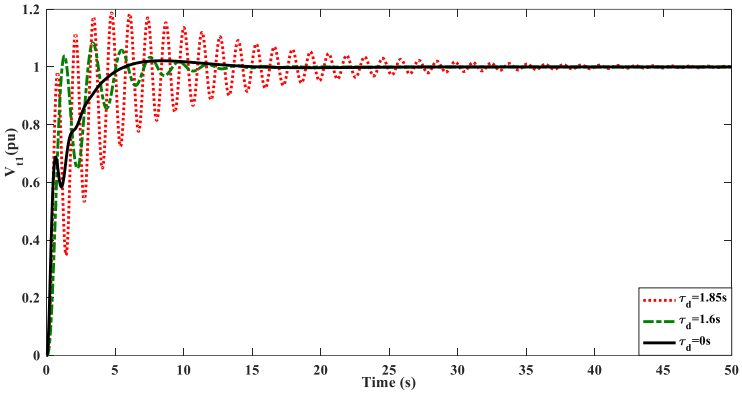

(**d**)

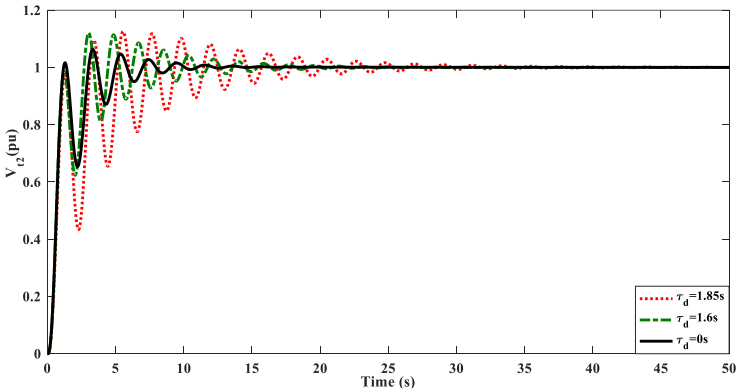

(**e**)

Figure 12. Dynamic responses with different time delays (τ_d) (**a**) Δf_1; (**b**) Δf_2; (**c**) ΔP_{tie}; (**d**) V_{t1}; (**e**) V_{t2}.

Figure 13. OPAL-RT lab setup with host PC.

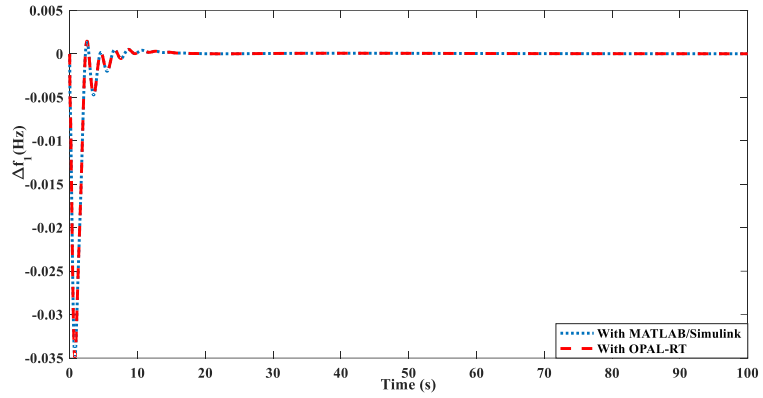

(**a**)

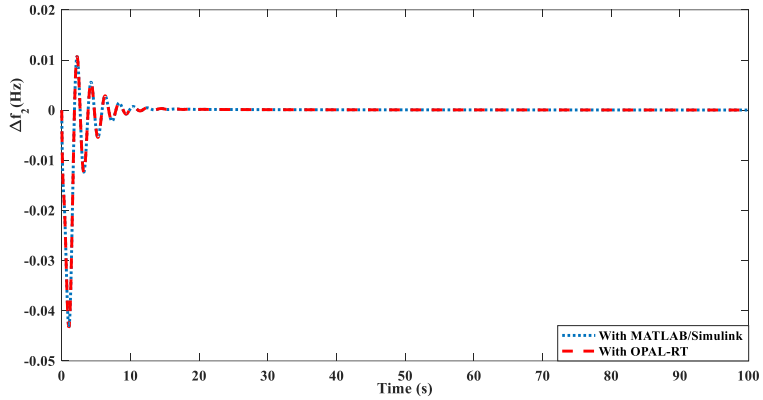

(**b**)

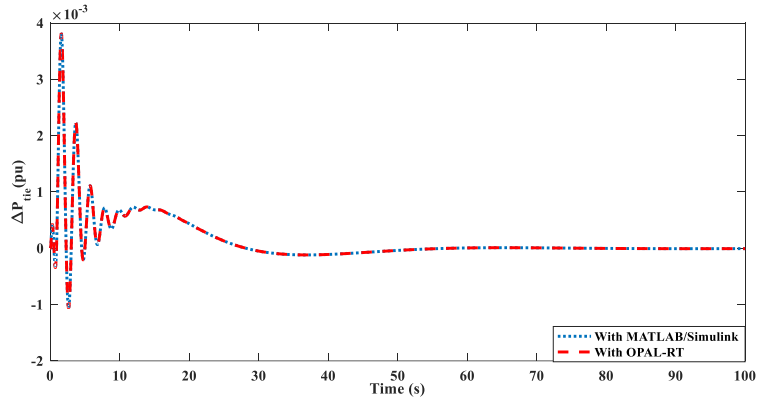

(**c**)

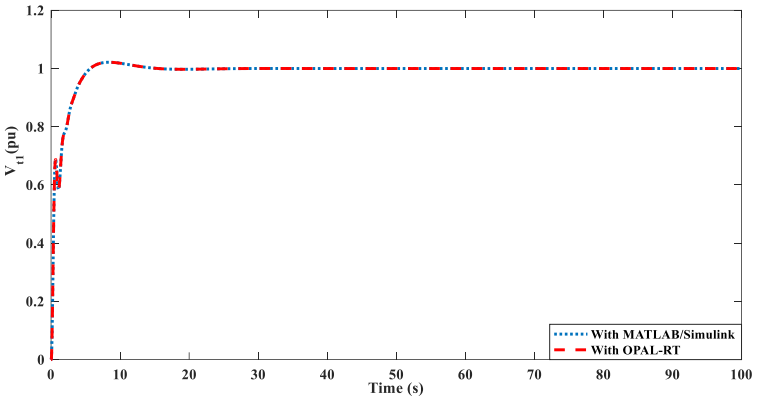

(**d**)

Figure 14. *Cont.*

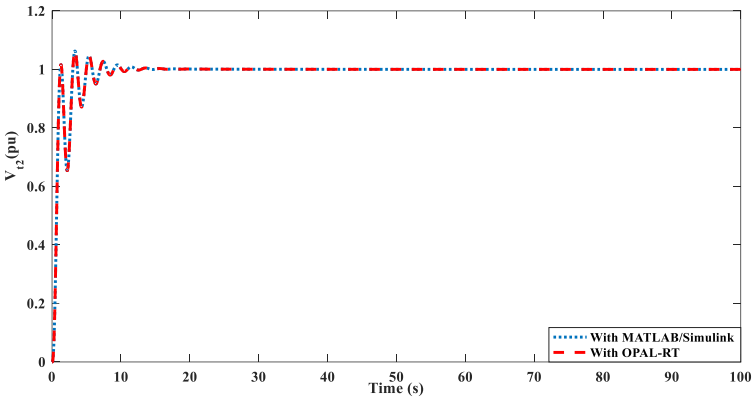

(**e**)

Figure 14. Validation of response through OPAL-RT OP4510: (**a**) Δf_1; (**b**) Δf_2; (**c**) ΔP_{tie}; (**d**) V_{t1}; (**e**) V_{t2}.

6. Conclusions

In this paper, the suppression of oscillations in the dynamics of the combined AGC and AVR system are performed utilizing a coot algorithm-tuned CPID-FOPID controller on the study considering two equal-area power systems with the following sources: reheat thermal power plant (RTPP) in addition to GRC, geothermal power plant (GTPP), solar thermal power plant (STPP), solar photovoltaic (SPV), and wind turbine generation (WTG). In this study, the power system was penetrated with electric vehicles (EVs) in both areas that serve as sources for the grid (V2G mode). The main findings of this research are explained below.

- The analysis revealed that the proposed cascaded controller is superior to the PID and FOPID controllers in terms of peak overshoot (M_P), peak undershoot (U_P), and settling time (T_s) when optimized using the coot algorithm.
- To verify the stability of the controller, the power system is also examined with realistic approaches, such as random load demand (RLD), fluctuating solar irradiances, and irregular wind powers. Even under these more real circumstances, the cascaded controller is superior to the FOPID controller.
- For the purpose of verifying the proposed controller's efficacy, a sensitivity analysis is conducted in which the RTPP and GTPP turbine time constants are varied by $+/-30\%$. This case study successfully confirms the CPID-FOPID controller capacity to survive these fluctuations, as the dynamics obtained under these conditions were found to be identical to those in the nominal case.
- The SMES-GCSC-SMES coordination is successfully verified with the CPID-FOPID controller.
- Moving toward a more realistic scenario, this article also addressed the impact of communication time delay, which degrades the system's dynamics when introduced into the system.
- The obtained simulation findings are successfully verified with validation using OPAL-RT OP4510 real-time digital simulator.

However, the research presented in this manuscript is limited to conventional power system, and the restructured AGC or combined AGC-AVR problem can be evaluated using the proposed coot algorithm-tuned cascaded controller. As the fuzzy logic controller provides superior performance, the combination of cascaded fuzzy-based controllers can be tested for the frequency and voltage regulation in an interconnected power system. As the number of tunable parameters are more in the fractional or cascaded controller, proper care should be taken when optimizing these controllers. The above-mentioned controllers can be designed utilizing the more efficient optimization technique, which delivers competitive global optimum results.

Author Contributions: Conceptualization, H.S. and M.R.; data curation, S.N., P.K. and A.S.R.; formal analysis, M.R. and P.K.; funding acquisition, H.S. and M.R.; methodology, H.S., M.R., P.K. and A.S.R.; project administration, S.N. and A.S.R.; resources, H.S. and M.R.; software, P.K. and S.N.; supervision, P.K. and S.N.; validation, H.S. and M.R.; visualization, A.S.R. and P.K.; writing—original draft, H.S. and M.R.; writing—review and editing, P.K., S.N. and A.S.R. All authors have read and agreed to the published version of the manuscript.

Funding: This research received no external funding.

Institutional Review Board Statement: Not applicable.

Informed Consent Statement: Not applicable.

Data Availability Statement: None.

Conflicts of Interest: The authors declare no conflict of interest.

Appendix A

Reheat Thermal Power Plant:
Governor time constant (T_g) = 0.08 s,
Turbine time constant (T_t) = 0.3 s,
Reheater gain (K_r) = 0.5,
Reheater time constant (T_{rt}) = 10 s.
Geothermal Power Plant:
Governor time constant (T_g) = 0.05 s,
Turbine time constant (T_t) = 0.1 s.
Solar Thermal Power plant:
Solar collector gain (K_{si}) = 1,
Solar collector time constant (T_{si}) = 1,
Governor time constant (T_{sg}) = 0.08 s,
Turbine time constant (T_{st}) = 3 s.
Power System:
Power system gain (K_P) = 120,
Power system time constant (T_P) = 20 s,
Synchronizing coefficient (T_{12}) = 0.0707 puMW/rad.
Electric Vehicle:
Gain (K_{EV}) = 1,
Time constant (T_{EV}) = 1 s.
Solar Photovoltaic:
Gain (K_{PV}) = 1,
Time constant (T_{PV}) = 1.8 s.
Wind Turbine Generator:
Gain (K_{WTG}) = 1,
Time constant (T_{WTG}) = 1.5 s
Automatic Voltage Regulator:
Amplifier gain (K_a) = 10,
Amplifier time constant (T_a) = 0.1 s,
Exciter gain (K_e) = 1,
Exciter time constant (T_e) = 0.4 s,
Generator field circuit gain (K_f) = 0.8,
Generator field circuit time constant (T_f) = 1.4,
Sensor gain (K_s) = 1,
Sensor time constant (T_s) = 0.05 s,
Cross-coupling coefficients of AVR: K_1 =1, K_2 = 0.1, K_3 = 0.5, K_4 = 1.4, and P_S = 0.145.
GCSC:
Gain (K_{GCSC}) = 1,
Time constant (T_{GCSC}) = 0.015 s
Controller:
${K_D}^w$, ${K_I}^w$, and ${K_P}^w$ denote the derivative, integral, and proportional gains in area w, respectively.
λ and μ represent the powers of integral and proportional gains, respectively.

References

1. Shukla, H.; Nikolovski, S.; Raju, M.; Rana, A.S.; Kumar, P. A Particle Swarm Optimization Technique Tuned TID Controller for Frequency and Voltage Regulation with Penetration of Electric Vehicles and Distributed Generations. *Energies* **2022**, *15*, 8225. [CrossRef]
2. Kalyan, C.N.S.; Goud, B.S.; Reddy, C.R.; Bajaj, M.; Sharma, N.K.; Alhelou, H.H.; Siano, P.; Kamel, S. Comparative Performance Assessment of Different Energy Storage Devices in Combined LFC and AVR Analysis of Multi-Area Power System. *Energies* **2022**, *15*, 629. [CrossRef]
3. Hossam-Eldin, A.A.; Negm, E.; Ragab, M.; AboRas, K.M. A Maiden Robust FPIDD2 Regulator for Frequency-Voltage Enhancement in a Hybrid Interconnected Power System Using Gradient-Based Optimizer. *Alex. Eng. J.* **2022**, *in press*. [CrossRef]
4. Kumar, V.; Sharma, V.; Naresh, R. Leader Harris Hawks Algorithm Based Optimal Controller for Automatic Generation Control in PV-Hydro-Wind Integrated Power Network. *Electr. Power Syst. Res.* **2023**, *214*, 108924. [CrossRef]
5. Singh, B.; Slowik, A.; Bishnoi, S.K. A Dual-Stage Controller for Frequency Regulation in a Two-Area Realistic Diverse Hybrid Power System Using Bull–Lion Optimization. *Energies* **2022**, *15*, 8063. [CrossRef]
6. Naveed, A.; Sonmez, S.; Ayasun, S. Impact of Electric Vehicle Aggregator with Communication Time Delay on Stability Regions and Stability Delay Margins in Load Frequency Control System. *J. Mod. Power Syst. Clean Energy* **2021**, *9*, 595–601. [CrossRef]
7. Tripathi, S.; Singh, V.P.; Kishor, N.; Pandey, A.S. Load Frequency Control of Power System Considering Electric Vehicles' Aggregator with Communication Delay. *Int. J. Electr. Power Energy Syst.* **2023**, *145*, 108697. [CrossRef]
8. Khan, M.; Sun, H. Complete Provision of MPC-Based LFC By Electric Vehicles with Inertial and Droop Support from DFIG-Based Wind Farm. *IEEE Trans. Power Deliv.* **2022**, *37*, 716–726. [CrossRef]
9. Khan, M.; Sun, H.; Xiang, Y.; Shi, D. Electric Vehicles Participation in Load Frequency Control Based on Mixed H2/H∞. *Int. J. Electr. Power Energy Syst.* **2021**, *125*, 106420. [CrossRef]
10. Debbarma, S.; Dutta, A. Utilizing Electric Vehicles for LFC in Restructured Power Systems Using Fractional Order Controller. *IEEE Trans. Smart Grid* **2017**, *8*, 2554–2564. [CrossRef]
11. Ramoji, S.K.; Saikia, L.C. Utilization of Electric Vehicles in Combined Voltage-frequency Control of Multi-area Thermal- Combined Cycle Gas Turbine System Using Two Degree of Freedom Tilt-integral-derivative Controller. *Energy Storage* **2021**, *3*, 1–20. [CrossRef]
12. Morsali, J. Fractional Order Control Strategy for Superconducting Magnetic Energy Storage to Take Part Effectually in Automatic Generation Control Issue of a Realistic Restructured Power System. *J. Energy Storage* **2022**, *55*, 105764. [CrossRef]
13. Nandi, M.; Shiva, C.K.; Mukherjee, V. Frequency Stabilization of Multi-Area Multi-Source Interconnected Power System Using TCSC and SMES Mechanism. *J. Energy Storage* **2017**, *14*, 348–362. [CrossRef]
14. Bhatt, P.; Roy, R.; Ghoshal, S.P. Comparative Performance Evaluation of SMES-SMES, TCPS-SMES and SSSC-SMES Controllers in Automatic Generation Control for a Two-Area Hydro-Hydro System. *Int. J. Electr. Power Energy Syst.* **2011**, *33*, 1585–1597. [CrossRef]
15. Pilla, R.; Azar, A.T.; Gorripotu, T.S. Impact of Flexible AC Transmission System Devices on Automatic Generation Control with a Metaheuristic Based Fuzzy PID Controller. *Energies* **2019**, *12*, 4193. [CrossRef]
16. Raju, M.; Saikia, L.C.; Sinha, N. Load Frequency Control of a Multi-Area System Incorporating Distributed Generation Resources, Gate Controlled Series Capacitor along with High-Voltage Direct Current Link Using Hybrid ALO-Pattern Search Optimised Fractional Order Controller. *IET Renew. Power Gener.* **2019**, *13*, 330–341. [CrossRef]
17. Oshnoei, S.; Oshnoei, A.; Mosallanejad, A.; Haghjoo, F. Contribution of GCSC to Regulate the Frequency in Multi-Area Power Systems Considering Time Delays: A New Control Outline Based on Fractional Order Controllers. *Int. J. Electr. Power Energy Syst.* **2020**, *123*, 106197. [CrossRef]
18. Oshnoei, A.; Kheradmandi, M.; Khezri, R.; Mahmoudi, A. Robust Model Predictive Control of Gate-Controlled Series Capacitor for LFC of Power Systems. *IEEE Trans. Industr. Inform.* **2021**, *17*, 4766–4776. [CrossRef]
19. Dekaraja, B.; Saikia, L.C. Combined Voltage and Frequency Control of Multiarea Multisource System Using CPDN-PIDN Controller. *IETE J. Res.* **2021**, 1–16. [CrossRef]
20. Kalyan, C.H.N.S.; Rao, G.S. Impact of Communication Time Delays on Combined LFC and AVR of a Multi-Area Hybrid System with IPFC-RFBs Coordinated Control Strategy. *Prot. Control. Mod. Power Syst.* **2021**, *6*, 1–20. [CrossRef]
21. Sahoo, S.C.; Barik, A.K.; Das, D.C. Synchronized Voltage-Frequency Regulation in Sustainable Microgrid Using Novel Green Leaf-Hopper Flame Optimization. *Sustain. Energy Technol. Assess.* **2022**, *52*, 102349. [CrossRef]
22. Abubakr, H.; Vasquez, J.C.; Hassan Mohamed, T.; Guerrero, J.M. The Concept of Direct Adaptive Control for Improving Voltage and Frequency Regulation Loops in Several Power System Applications. *Int. J. Electr. Power Energy Syst.* **2022**, *140*, 108068. [CrossRef]
23. Ramoji, S.K.; Saikia, L.C. Maiden Application of Fuzzy-2DOFTID Controller in Unified Voltage-Frequency Control of Power System. *IETE J. Res.* **2021**, 1–22. [CrossRef]
24. Ramoji, S.K.; Saikia, L.C. Optimal Coordinated Frequency and Voltage Control of CCGT-Thermal Plants with TIDF Controller Optimal Coordinated Frequency and Voltage Control of CCGT-Thermal Plants with TIDF Controller. *IETE J. Res.* **2021**, 1–18. [CrossRef]
25. Mok, R.; Ahmad, M.A. Fast and Optimal Tuning of Fractional Order PID Controller for AVR System Based on Memorizable-Smoothed Functional Algorithm. *Eng. Sci. Technol. Int. J.* **2022**, *35*, 101264. [CrossRef]

26. Kumar, A.; Pan, S. Design of Fractional Order PID Controller for Load Frequency Control System with Communication Delay. *ISA Trans.* **2022**, *129*, 138–149. [CrossRef]
27. Li, M.; Du, W.; Nian, F. An Adaptive Particle Swarm Optimization Algorithm Based on Directed Weighted Complex Network. *Math. Probl. Eng.* **2014**, *2014*. [CrossRef]
28. Elgamal, Z.M.; Yasin, N.B.M.; Tubishat, M.; Alswaitti, M.; Mirjalili, S. An Improved Harris Hawks Optimization Algorithm with Simulated Annealing for Feature Selection in the Medical Field. *IEEE Access* **2020**, *8*, 186638–186652. [CrossRef]
29. Naruei, I.; Keynia, F. A New Optimization Method Based on COOT Bird Natural Life Model. *Expert Syst. Appl.* **2021**, *183*, 115352. [CrossRef]